Small

NANO · MICRO small
www.small-journal.com

RESEARCH ARTICLE

Nanoscale Evidence of Junction-Limited Transport in $Ti_3C_2T_x$ MXene

Oriane de Leuze[1] | Maxime Berthe[2] | Sophie Hermans[1] | Benoît Hackens[1]

[1]IMCN, UCLouvain, Louvain-La-Neuve, Belgium | [2]University Lille, CNRS, Centrale Lille, University Polytechnique Hauts-de-France, Lille, France

Correspondence: Benoît Hackens (benoit.hackens@uclouvain.be)

Received: 18 November 2025 | **Revised:** 20 February 2026 | **Accepted:** 24 February 2026

Keywords: charge transport | humidity sensing | junction resistance | MXenes | nanoscale

ABSTRACT

Understanding charge transport in networks of 2D crystals is essential for developing reliable applications such as chemiresistors or electromagnetic shields. For this purpose, intra- and inter-flake contributions to the network resistance must be disentangled. MXenes such as $Ti_3C_2T_x$, are prime examples of 2D crystals often employed as thin networks of interconnected flakes for functional devices. While a significant number of studies focused on transport in individual MXene flakes, inter-flake transport remains scarcely explored. Here, we demonstrate that charge transport in multi-flake conductive paths of $Ti_3C_2T_x$ is dominated by interflake junctions and provide quantitative estimates of junction resistances. Scanning probe measurements reveal that in a MXene multi-flake conductive path, individual flakes behave as isopotential domains, since the voltage drop is localized precisely at inter-flake junctions. The chemiresistive response to humidity is further investigated at the single flake, multi-flake and flake network scale, evidencing the crucial impact of junctions on sensing kinetics. These findings underline the dominant role of inter-flake junctions in MXene charge transport and sensing capabilities.

1 | Introduction

Scalability has been an ongoing challenge since the birth of 2D crystals with exfoliated graphene. Now, solution-processed layers of 2D crystals are increasingly used in electronics as they comply with standard microfabrication techniques and are compatible with various substrates, from silicon to textile. The target applications for such 2D layers include flexible electronics, sensors, or logic devices [1]. For this, the main deposition techniques that comply with solution-processed 2D crystals rely on inkjet printing, drop casting, spray-coating and spin coating, yielding thin films formed by networks of overlapping flakes [2, 3]. The obtained layers are shown to be very disordered as flake stacking and orientation are uncontrolled. Also, flake size can be rather disperse in a suspension, increasing the random, fragmented nature of the deposited layer. Understanding charge transport in those layers is therefore challenging but necessary to tune their electrical properties depending on the target application.

A way to gain more insight about charge transport in the case of nanosheet networks is to consider the network as many well-defined conductive paths in parallel. This approach was used by Gabbett et al. to describe network resistivity and mobility as functions of network properties such as flake thickness and channel length [4]. In this model, each conductive path consists of a series of resistors including nanosheet resistance, R_{NS} and junction resistance between the nanosheets, R_J. This flake-junction distinction is a key-element in how to approach charge transport in 2D materials, as it underlines the need to understand not only intra-flake but also inter-flake transport mechanisms [5]. Extracting meaningful data on junctions is not trivial due to the many unknowns that include the voltage drop profile in the vicinity of the junction, the configuration of current paths,

the particular stacking configuration, the role of functionalization groups and defects at the edge of the flakes, as well as the nanoscale dimensions. Such scales can typically be reached with scanning probe microscopy tools, but the problem complexity calls for an approach involving different scanning probe modes.

In this work, we focus on the case of $Ti_3C_2T_x$, the most widely studied and well-known MXene to date. MXenes are a family of 2D transition metal carbides, nitrides and carbonitrides, which are obtained by selective etching and delamination of a 3D lamellar MAX precursor [6]. There is a considerable interest in MXenes due to their tunable chemical and electronic properties, as their rich surface chemistry can be tuned depending on the synthesis parameters [7]. Those surface groups are noted T_x in the general MXene formula, which is $M_{n+1}X_nT_x$, where "M" represents the transition metal, "X" is either carbon or nitrogen and "n" = 1, 2 or 3. Also, the wide range of possible combinations of different transition metals and functional groups makes MXenes a highly versatile material family. $Ti_3C_2T_x$ was the first MXene to be synthesized in 2011 and shows now great promise in the fields of flexible electronics, electromagnetic interference shielding, energy storage, and sensing [8–12]. In those applications, MXenes are mostly used as "films". In a recent review, Barsoum and Gogotsi insist on the importance of decoupling inter- and intra-flake charge transport in order to gain more control on the electronic properties of those films [13]. Here, it is worth to note that a distinction has to be made between spin-coated films and those which are drop-cast or filtered, as the alignment between the flakes in spin-coated films shows less variability in the quantitative results from one work to another, regarding electrical properties such as conductivity and mobility. This distinction makes it even more interesting to consider the problem at flake-scale. Yet, such scales are challenging to reach given the small lateral size of the flakes, requiring scanning probe microscopies or microfabrication processes to pattern contacts on the areas of interest [14, 15].

To date, several studies have been carried out on individual flakes, both at room and low temperature, shedding light on transport mechanisms in $Ti_3C_2T_x$ [16–20]. There is an agreement in literature about the all-time metallic nature of $Ti_3C_2T_x$ and about the fact that the individual flake conductivity will directly be affected by the amount of defects and oxidation state of the flake [18, 19, 21]. Although the understanding of transport in individual flakes is increasing, studies that include inter-flake transport are very scarce. A recent work evaluates the layer-dependent sensing characteristics of MXenes at flake-scale and includes both individual flakes and inter-flake junctions, shedding light on specific and contrasting sensing mechanisms in both cases [22]. Such a pioneering result further underscores the need for flake-scale experimental characterization as a tool to develop and understand MXenes-based electronic applications.

In this context, we leveraged different methods to study charge transport at the nanoscale within individual few-layer $Ti_3C_2T_x$ flakes and across the junction between flakes. Herein, electrical-mode scanning probe microscopies and measurements on patterned devices are combined to reach quantitative conclusions and local insights. Lastly, electrical responses to humidity at the intra-flake, inter-flake, and flake network scales reveal different characteristic time scales, relevant in the context of sensing applications involving MXenes.

2 | Results and Discussion

$Ti_3C_2T_x$ MXene flakes are synthesized using the MILD method, yielding high quality 2D crystals suitable for transport measurements at the individual flake scale level. Structural characterization by X-ray diffraction shown in Figure S9b (Supporting Information) reveals a c lattice parameter of 25.2 Å, which is in the range of previous report using HCl-LiF etching for MXene synthesis [23]. The "Tx" groups are dominated by –O, –OH and –F terminations, as confirmed by X-ray photoelectron spectroscopy (XPS) and Raman spectroscopy which are provided in the Supporting Information Section S7. By comparing SEM images and XPS quantification of the MAX precursor [24] and the obtained MXenes, we confirmed the successful removal of the Al layer and the complete delamination of the 3D lamellar structure of Ti_3AlC_2 into separate 2D layers.

2.1 | 4-Probe STM on the Individual Flake

A multiple-probe Scanning Tunneling Microscope (STM) is used to perform 4-contact measurements on $Ti_3C_2T_x$ few-layer flakes, lying on an insulating substrate (SiO_2-covered Si) as illustrated in Figure 1. High reliability of the data and stability between different measurements are obtained due to the ultrahigh vacuum (UHV) STM environment, the accuracy of tip-flake contact position and the inter-tip distance that can reach values below 100 nm. These conditions are allowed by the sharp geometry of STM tips that have a nm-sized apex and the controlled displacement of the probes under scanning electron microscope visualization.

The first experiment carried out is a 4-contact measurement on an individual flake with a homogeneous topography, as depicted in Figure 1a, that shows a 3-D view of the AFM topography of the flake. Figure 1c displays the thickness profile extracted along the white dotted line in (a), confirming the topography homogeneity. The four STM probes are positioned on the flake along a straight line as shown on the SEM image in Figure 1d. In this configuration, the current is applied between the two outer probes and the voltage drop measured between the two inner probes, whose spacing is 1.8 μm. The flake-resistivity can then be extracted from the current-voltage characteristics shown in Figure 1b. Those are linear and show no hysteresis, which is expected due to the metallic nature of $Ti_3C_2T_x$. Knowing the spacing between the probes d, the in-plane resistivity value of the flake is obtained by matching the experimental results with a COMSOL finite element simulation: $\rho_{xx} = 6.06\ \Omega \cdot \mu m$. An image of the simulated potential distribution on the flake is shown in the Supporting Information S1. The use of a finite element simulation is needed here as the size of the flake is in the same range as the probe spacing, which prevents the use of conventional 4-point probe expressions to compute the flake resistivity.

The resistivity value obtained here is in agreement with a previous work that reports resistivity values for individual few-layer $Ti_3C_2T_x$ flakes in ambient conditions [12]. Those values are represented on a graph along with flake thickness in the

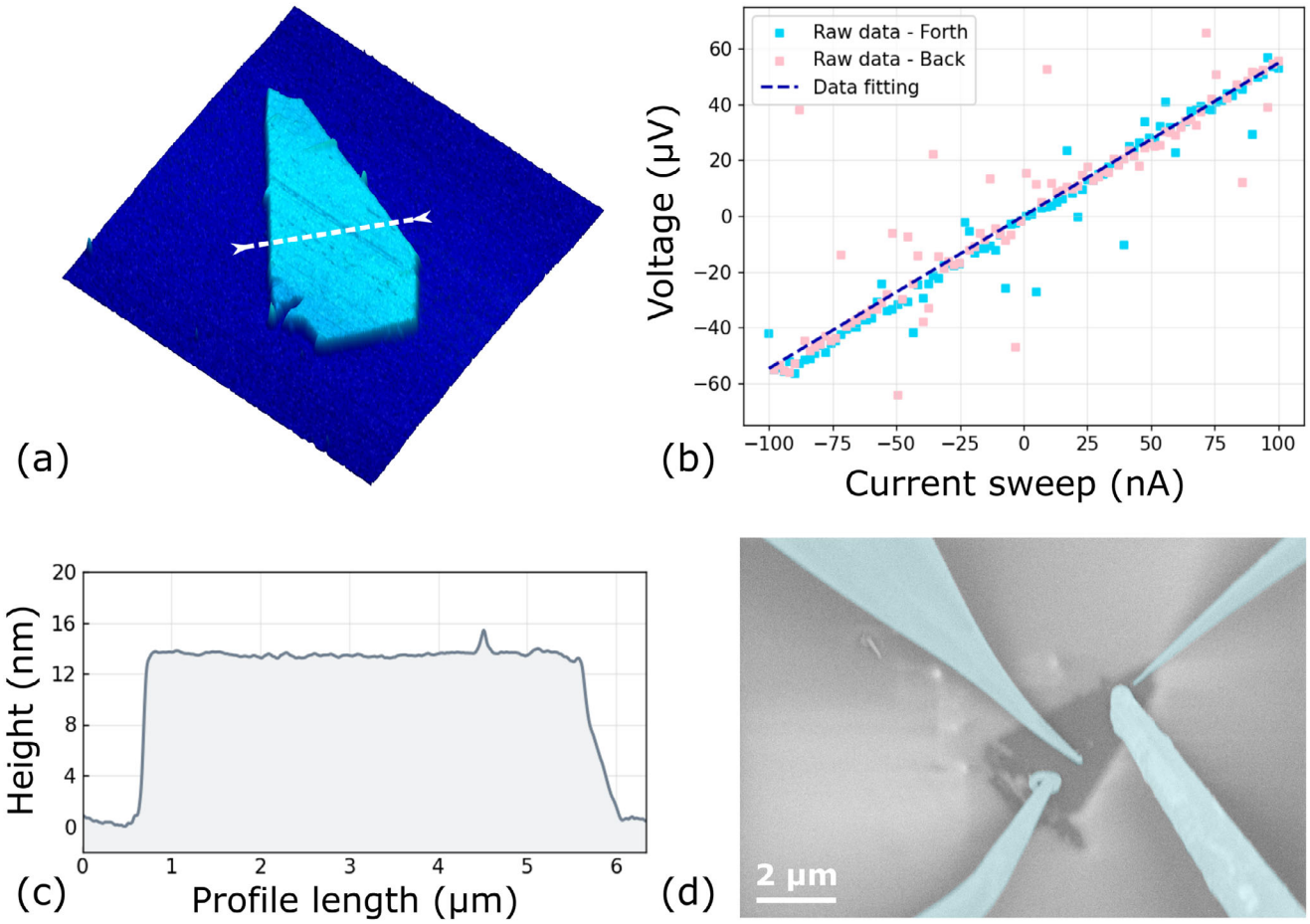

Figure 1 | (a) 3D view of the AFM topography of a $Ti_3C_2T_x$ flake deposited on a Si/SiO_2 substrate, obtained in tapping mode. (b) I–V characteristic obtained by 4-probe measurement on the flake shown in (a). (c) Height profile along the white dotted line in (a). (d) SEM image of the $Ti_3C_2T_x$ with the tungsten probes placed in the 4-contact measurement configuration.

Supporting Information S1. This first result validates the 4-probe STM approach to extract quantitative electrical measurements on $Ti_3C_2T_x$ flakes and suggests that the in-plane resistivity of $Ti_3C_2T_x$ does not vary significantly in UHV environment, compared to ambient air conditions. Contact resistance is also measured by comparing 2- and 4- contact measurements and is about 2.5 kΩ in this case, highlighting the necessity to perform 4-contact measurements. More details are shown in the Supporting Information S2.

2.2 | 4-Probe STM on a Conductive Path

Following intra-flake measurement, we consider the case of a conductive path made of four overlapping individual MXene flakes. This configuration is illustrated in the 3-D view of the topography of the sample in Figure 2a and its thickness profile in Figure 2b along the white dashed line in Figure 2a. The conductive path established through these four flakes allows to study each junction separately with the four-probe STM. Hence, four-contact measurements were carried on along the conductive path at different locations, as showcased in Figure 2c,d, where the indicated distance corresponds to the spacing between measuring probes. The two outer probes are applying a fixed current through the conductive path and only one of the measuring probes is displaced for each measurement point. Similarly to the measurement on an individual flake, an IV curve is acquired for every measurement point.

Figure 2e displays the IV characteristics corresponding to the two measurements configuration shown by the SEM micrographs in Figure 2c,d. Both are linear, which means that electronic transport through flake junctions is still ohmic. Also, the resistance increases along the conductive path as the distance between the measuring probes is increased. The resistance profile can be further assessed by performing multiple measurements along the conductive path, represented by the white squares in Figure 2c. In Figure 2f, we clearly see that the resistance increase occurs by steps corresponding to the location of inter-flake junctions. Hence, inter-flake junction resistances R_{J1}, R_{J2} and R_{J3} are the main contributions to the total resistance measured along the conductive path.

2.3 | Scanning Tunneling Potentiometry on an Inter-Flake Junction

As suggested by the steps shown in Figure 2f, the resistance increase appears to be sharp and very localized. To confirm this observation, Scanning Tunneling Potentiometry (STP)

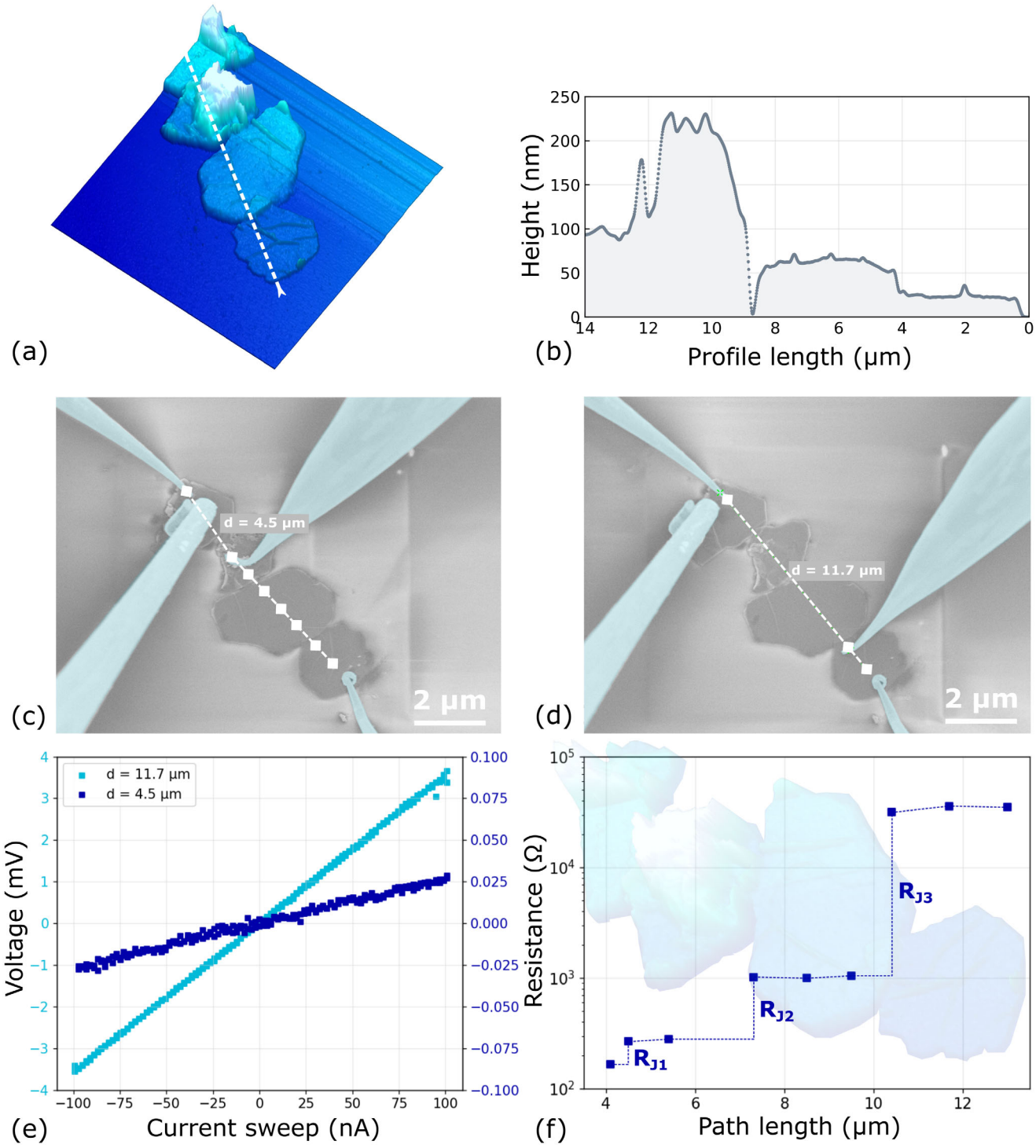

Figure 2 | (a) 3D view of the AFM topography of a conductive path formed by $Ti_3C_2T_x$ flakes deposited on a Si/SiO_2 substrate, obtained in tapping mode. (b) Height profile along the white dotted line in (a). (c,d) SEM images of the 4-probe measurement along the conductive path, for two different measurement points, with the distance between the measuring probes being 4.5 and 11.7 μm, respectively. (e) I–V characteristics for both measurements points shown in (c) and (d). Note that the vertical (voltage) scale for the light blue curve (left axis) is orders of magnitude larger than for the dark blue curve (right axis). (f) Electrical resistance along the conducting path as a function of the distance between the measuring probes.

measurements are carried out on the same sample, at the location corresponding to the third junction, represented as R_{J3} in Figure 2f. This junction was chosen as we can identify the region corresponding to a clear overlap between the flakes, with a limited amount of defects and wrinkles compared to the other junctions. STP yields a map of the local electrical potential while applying a given current on the sample with the two external STM probes [25]. This measurement configuration is shown in Figure 3a,c and the obtained maps of STM topography and potential voltage are acquired simultaneously and shown in Figure 3b. Interestingly, a sharp decrease in the measured potential is observed at the edge of the overlapping area of both flakes, further highlighted

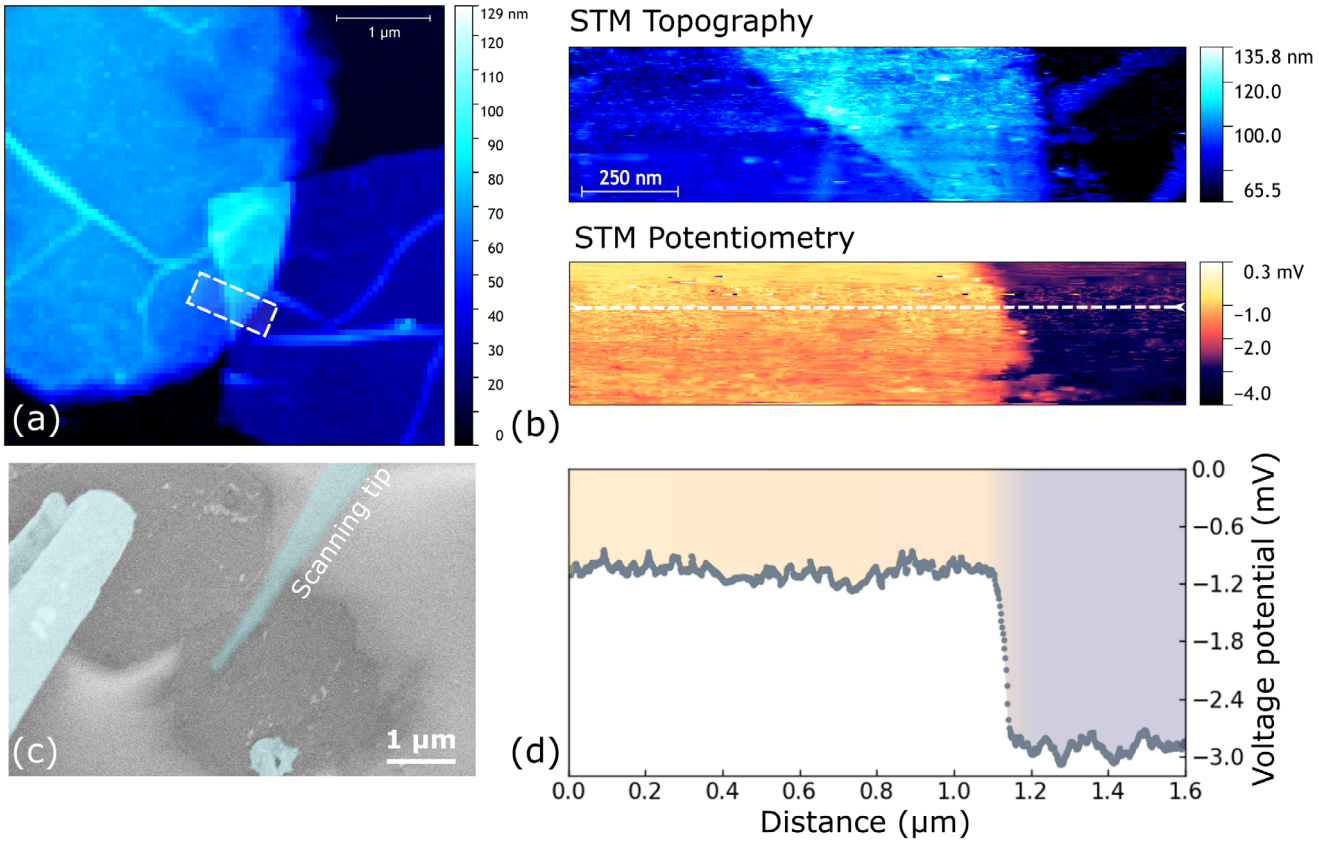

Figure 3 | (a) AFM topography of the junction resistance, obtained in tapping mode. (b) STM topography and potentiometry inside the rectangle highlighted in (a). (c) SEM image of the probe configuration of the potentiometry measurement obtained with a 100 nA current between the two outer probes. (d) Profile of the potential along the white dashed line in (b).

by the electrical potential profile in Figure 3d. Here, the potential is found to be approximately constant, and the voltage drop of 1.8 mV at the inter-flake junction is directly attributed to junction resistance. This resistance drop yields a value of 18.4 kΩ, which is close to the value of R_{J3} measured by 4-probe measurements. The difference between both values can be explained by the higher imprecision on the voltage measurement with STP than with 4-probe measurements, but STP really gives access to local resistance variations.

Those results are in agreement with Gabbett's description of a junction-limited network, and in line with previous Kelvin probe force microscopy (KPFM) results on a MoS_2 layer, where sharp changes in the surface potential were also attributed to junctions [4, 26]. The additional insight given by STP here is the ability to consider only one junction at once, with high precision of both current injection position and electrical potential measurement position.

2.4 | Conductive Path Devices

To get one step closer to contacted flake networks, charge transport is now studied in devices made of a conductive MXene path on which metallic contacts are patterned through a lift-off process. The contact geometry is designed to discriminate the measurements on individual flakes from those including a junction between two flakes. The AFM topography of such a device is presented in Figure 4a, which shows three individual flakes forming a conductive path (different from the one presented in Figure 2), covered with 7 metallic contacts. This specific geometry allows to perform 4-contact measurements on both individual flakes and inter-flake junctions. The sample was measured in ambient conditions and exhibited increased resistance values on the segments including a junction, as shown by the graph in Figure 4b. Here, R_{J1} = 1.9 kΩ and R_{J2} = 18.4 kΩ, representing the two junction resistances as indicated in Figure 4a,b. The inset of Figure 4b shows that linear IV curves are obtained both on sections including junctions and individual flakes. The resistance values obtained as well as the IV curves linearity are consistent with the 4-probe STM results presented above, despite a difference in the measurement conditions as the devices are measured at ambient conditions here, compared to UHV above. In both cases, it appears that junctions are the main resistive component of the conductive path.

Now, we discuss the origin of the high junction resistances. Despite their high resistance, inter-flake junctions in $Ti_3C_2T_x$ remain in a metallic regime, as verified by the linear IV characteristics obtained with 4-probe STM (Figure 2e) and microfabricated devices (inset of Figure 4b). Also, multiple works report a positive $d\rho/dT$ on $Ti_3C_2T_x$ networks and individual flakes, which is consistent with a metallic regime [19, 27, 28]. High-junction resistance values are therefore not due to chemical barriers or tunneling at the junction interfaces, as those would

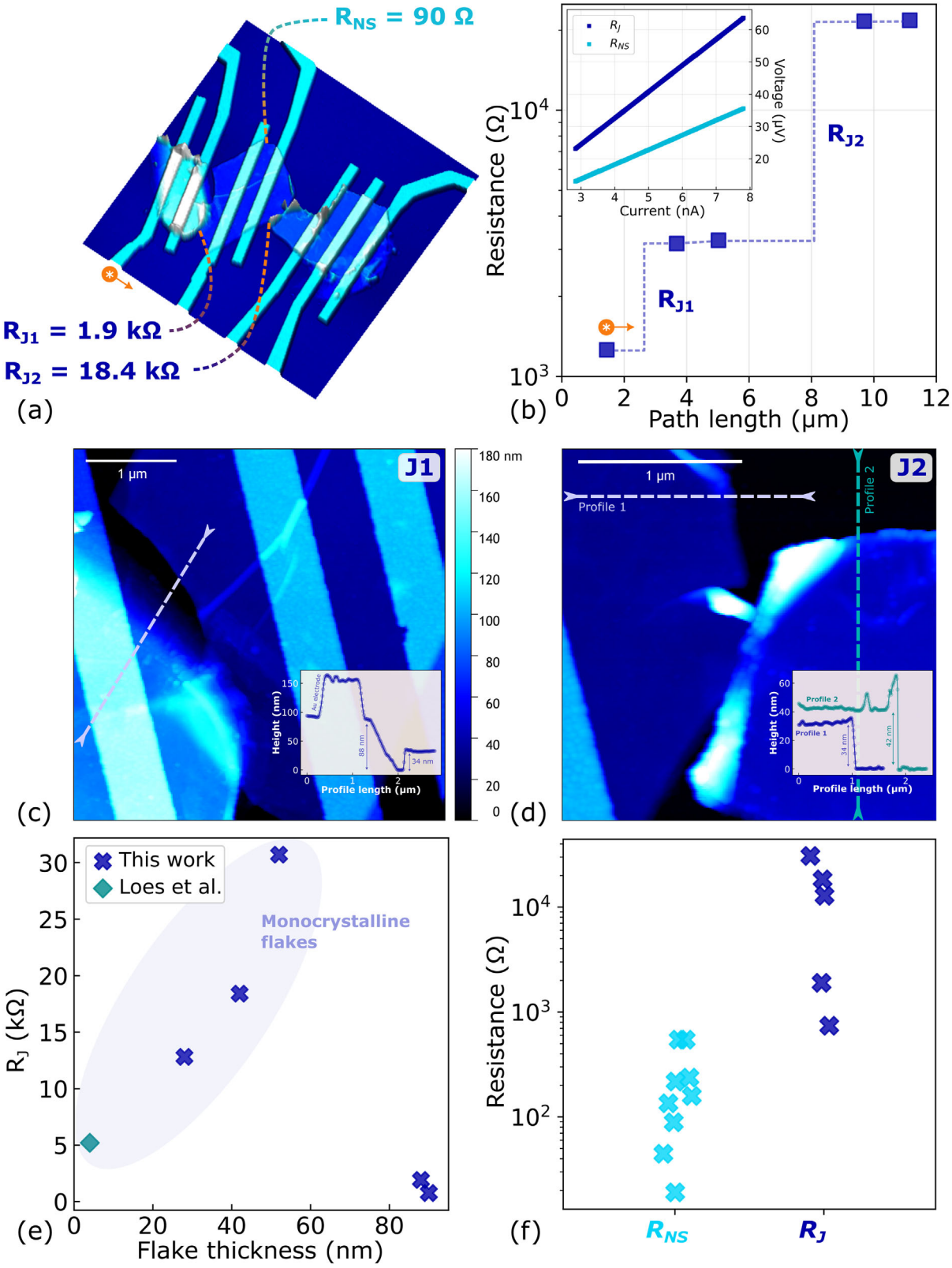

Figure 4 | (a) 3D view of the AFM topography of a device with metallic contacts on $Ti_3C_2T_x$ flakes, obtained in tapping mode. (b) Electrical resistance along the conducting path as a function of the distance between the measuring contacts. The inset shows I–V curves acquired on one junction and on the individual flake. (c,d) Topographical details of the junctions between the flakes of the device shown in (a). The insets show height profiles extracted at the locations indicated by the dashed lines on the AFM scans. (e) Junction resistance values, along with flake thickness, for this work and the value reported in Loes et al. [22]. (f) Resistance values obtained from 4-contact measurements on fabricated devices and 4-probe STM of individual flakes (R_{NS}) and inter-flake junctions (R_J). Note that the y-axis is in logarithmic scale for better visualization.

lead to Schottky-like I–V characteristics when measuring an inter-flake junction.

A closer look at the junction morphology is provided by the AFM topography maps shown in Figure 4c,d, where height profiles along the dashed lines are added in the insets. Such precise topographical details allow to evaluate the relation between junction resistance values and junction morphology, characterized typically by flake thickness and by the overlap area between the flakes. The junction resistance values obtained here are relatively independent of overlap area, as shown in the Supporting Information S4. However, it is important to note that the overlap area measured with AFM topography maps is not necessarily representative of the effective contact area between the flakes, as the latter can be modulated by the presence of wrinkles, defects or impurities between the flakes, that are difficult to observe. More generally, the high junction resistance could be partially ascribed to the presence of a constriction resistance that depends on the effective electrical contact area between the flakes and is usually described as $R_{spr} = \rho/2a$, where a is the contact radius and ρ the material resistivity [29].

When considering a typical junction between two microcrystalline flakes, the total resistance encompasses both in-plane and out-of-plane resistive components, as illustrated in the Supporting Information S3. The out-of-pane resistive component directly implies high resistance values, since the resistivity in MXenes is highly anisotropic. Previous works reported a resistivity anisotropy of about three orders of magnitude in $Ti_3C_2T_x$ [12, 30]. The contribution of high out-of-plane resistivity is further supported by the increase of junction resistance with flake thickness, as depicted in Figure 4e for monocrystalline flakes. An additional value from the work Loes et al. is shown on the same graph [22], and two measurements also show a lower junction resistance for thick (above 80 nm) and disordered flakes, which are distinct from the monocrystalline case. The increase in junction resistance with flake thickness observed here is consistent with the model of Gabbett and coworkers, in which the resistivity of a nanosheet network is expressed with a linear dependence on flake thickness [4]. Recent experimental results on spray-cast graphene nanosheet networks also confirm this linear dependence and fit this model [5].

It is then possible to ascribe the origin of high junction resistance values to a combination of a high out-of-plane resistivity of $Ti_3C_2T_x$ related to resistivity anisotropy and the constriction resistance depending on the effective electrical contact area at the flake interface.

All the resistance values obtained with 4-contact measurements on individual flakes (R_{NS}) and junctions (R_J) are represented in Figure 4f. While the dominance of R_J is clear as shown on the logarithmic scale, a significant spread in those values is observed. A part of this dispersion is likely related to the morphology of the measured device, especially for individual flakes which are less resistive. For junction resistances, we expect that morphological differences such as flake lateral size, overlap area and flake thickness have a dominant effect on the measured resistance. For example, several works show that the conductivity and sensing performances of a $Ti_3C_2T_x$ flake network can be tuned as a function of the network morphology [31]. As an example, Guo and coworkers show that they could overcome low intrinsic conductivity in transparent conductive electrodes by increasing flake size above 10 μm, decreasing the amount of junctions in the network, therefore limiting the contribution of out-of-plane resistivity [32]. Ultimately, gaining control on network morphology is likely to be a key-element to achieve a better reproducibility in MXenes network resistivity.

2.5 | C-AFM

In complement to the STP experiments, Conductive Atomic Force Microscopy (C-AFM) is performed on $Ti_3C_2T_x$ flakes deposited overlapping an insulating substrate and a metallic electrode, as presented in Figure 5a. Compared to STP, done in UHV, C-AFM measurements are performed in ambient conditions and have less stringent scan size limitations than STM, which allows to image several entire flakes at once. C-AFM allows simultaneous acquisition of a map of the sample topography and a map of the current flowing between the tip and sample, therefore allowing to image the sample conductivity changes. With this in mind, Figure 5b,c shows a C-AFM scan in which a junction between two flakes can be observed in a region where the C-AFM signal is stable. It is challenging to obtain quantitative findings based on the absolute current values measured in C-AFM as the 2-contact measurement (tip-sample) continuously evolves over time, tip state or humidity [33, 34].

Nevertheless, the current map obtained here with C-AFM reveal that the current values measured over the flake surfaces are homogeneous, while a drastic change occurs across flake junction. To gain more precise insight, we can extract a current profile in the area of interest, as depicted in Figure 5c,d and obtain the value of the current drop between the two flakes, which is about 130 nA. Additional C-AFM results and profiles show similar current drops at flake junctions and are presented in the Supporting Information S5. These results are in excellent agreement with STP presented above and demonstrate that a MXene conductive path can be considered as isopotential domains separated by junctions, in both UHV and ambient conditions. More generally, we conclude that the transport picture in UHV can also be considered as valid in ambient conditions, due to the good correspondence of both STP and C-AFM electrical profiles, and of the values extracted from 4-probe STM and patterned devices, on individual flakes and inter-flake junctions.

2.6 | Humidity Response of $Ti_3C_2T_x$

To Illustrate the profound impact of junctions on MXene electronic applications, we studied the effect of humidity on the conductance of $Ti_3C_2T_x$. For this, several devices involving different flake configurations have been exposed to various humidity levels in a N_2 atmosphere, in order to compare the case of an individual flake, two flakes including a junction, and a layer of networked flakes, as shown in Figure 6c,f,i. Here, each sample shows a distinct increase in resistance upon humidity exposure, as depicted in Figure 6a–h where the response is defined as $Resp = \frac{R_{hum} - R_{N2}}{R_{N2}}$. In this expression, R_{hum} is the measured resistance and R_{N2} is the baseline resistance after stabilization in N_2.

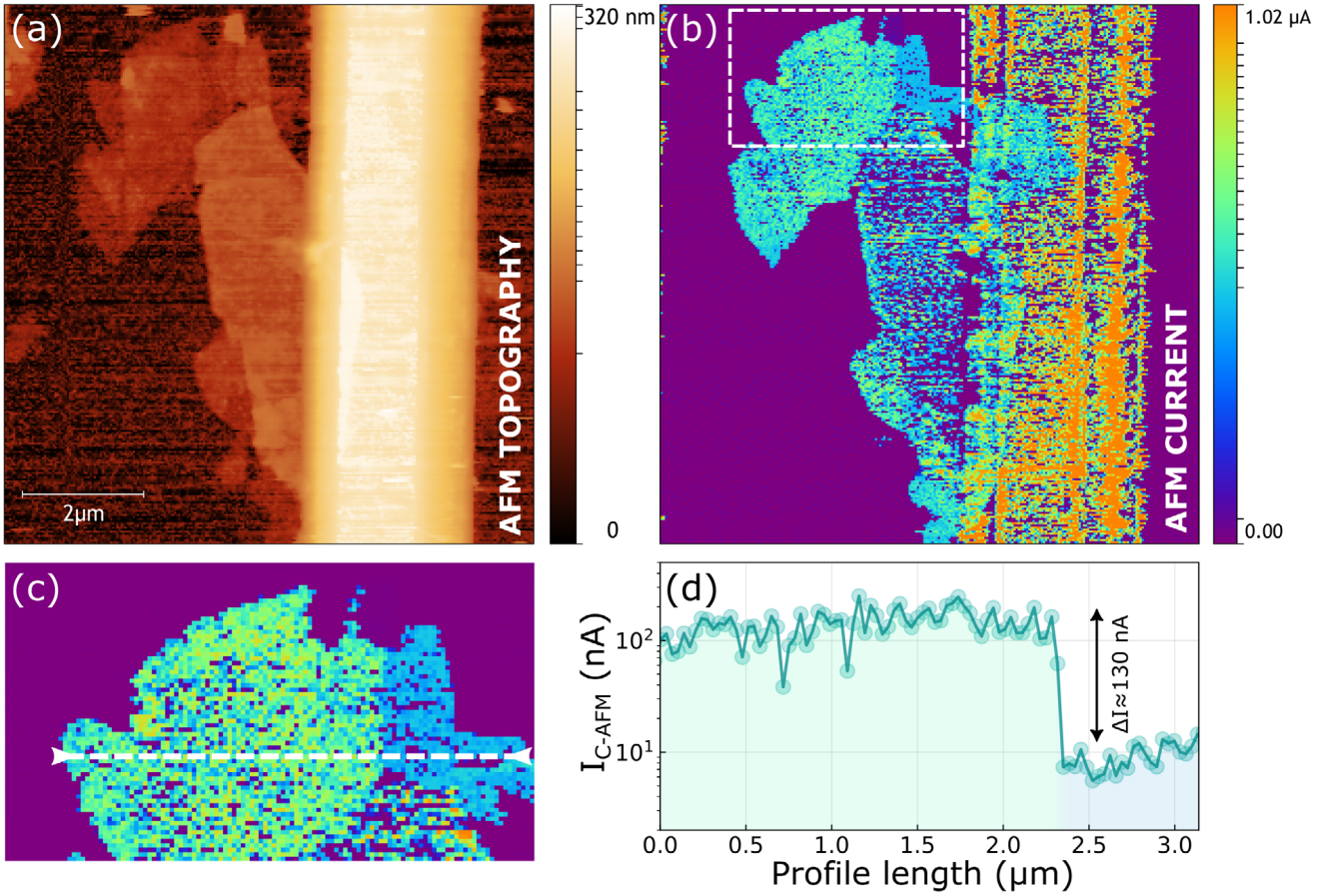

Figure 5 | (a) 3D view of the AFM topography and (b) current map of $Ti_3C_2T_x$ flakes overlapping a metallic electrode and an insulating substrate, obtained with Conductive AFM with a 3.5 mV bias between tip and sample. (c) Detail in the current map shown in (b). (d) C-AFM current profile along the white dotted line in (c), taken with a 5-pixel thickness (34 nm).

Several possible mechanisms have been discussed to explain the sensing response of MXenes, including charge transfer between the adsorbed molecules and $Ti_3C_2T_x$ and molecular intercalation between the MXene layers [35]. In a recent work on layer-dependent sensing mechanism in MXenes, Loes and coworkers show that the sensing behavior of a $Ti_3C_2T_x$ monolayer is intrinsically n-type, meaning that they exhibit a decrease in their electrical resistance under the exposure of reducing analytes [22]. In contrast, for bilayer structures made of two overlapping monolayers, they report a positive response for both reducing and oxidizing analytes, that they attribute mainly to molecular intercalation between the layers. Following this logic, the positive response observed for all the devices presented in Figure 6 suggests that the dominant contribution to the response is molecular intercalation, and shows that a distinction has to be made between individual monolayer flakes (negative response) and individual multilayer flakes (positive response). It is also important to note that the intercalation of water molecules is facilitated by the hydrogen bonding interactions between water and the termination groups, highlighting their essential role regarding MXene hydrophilicity and on a broader scale, gas sensing capabilities [36, 37].

It is worth noting that the dynamics of sensing also depends on the number of layers and their stacking. In our case, the sensing dynamics of the inter-flake junction is much faster than the one of the individual multilayer flake, as observed directly in Figure 6b,e. The response time, defined as the time to reach 90% of the maximal response, is of 606 s for the individual flake and of 61 s in the presence of an inter-flake junction. The comparatively slow response observed for the individual flake is consistent with diffusion-limited intercalation within a confined layered structure and can be accurately fitted with Fick's diffusion law, as depicted in Figure S11a. In contrast, the inter-flake junction shows a response nearly one order of magnitude faster, suggesting that this configuration provides more accessible pathways for water intercalation and removal. Also, it is expected that any modification in the junction interlayer spacing is sufficient to induce distinct changes in the overall resistance, given the junction-dominated transport described above.

Now, considering the case of a network of flakes shown in Figure 6g–i we observe that its sensing kinetics is close to the one of the inter-flake junction, with a response time of 44 seconds. Therefore, we conclude that the sensing kinetics of $Ti_3C_2T_x$ flake networks is likely dominated by inter-flake junctions. While most of the gas-sensing reports involving $Ti_3C_2T_x$ rely on its combination with other sensitive materials such as GO for improved performances,[38–40] it does not remove the need for fundamental understanding of the sensing characteristics of pristine MXenes at flake-scale. Further studies could investigate how the sensing performances of MXene layers are affected by

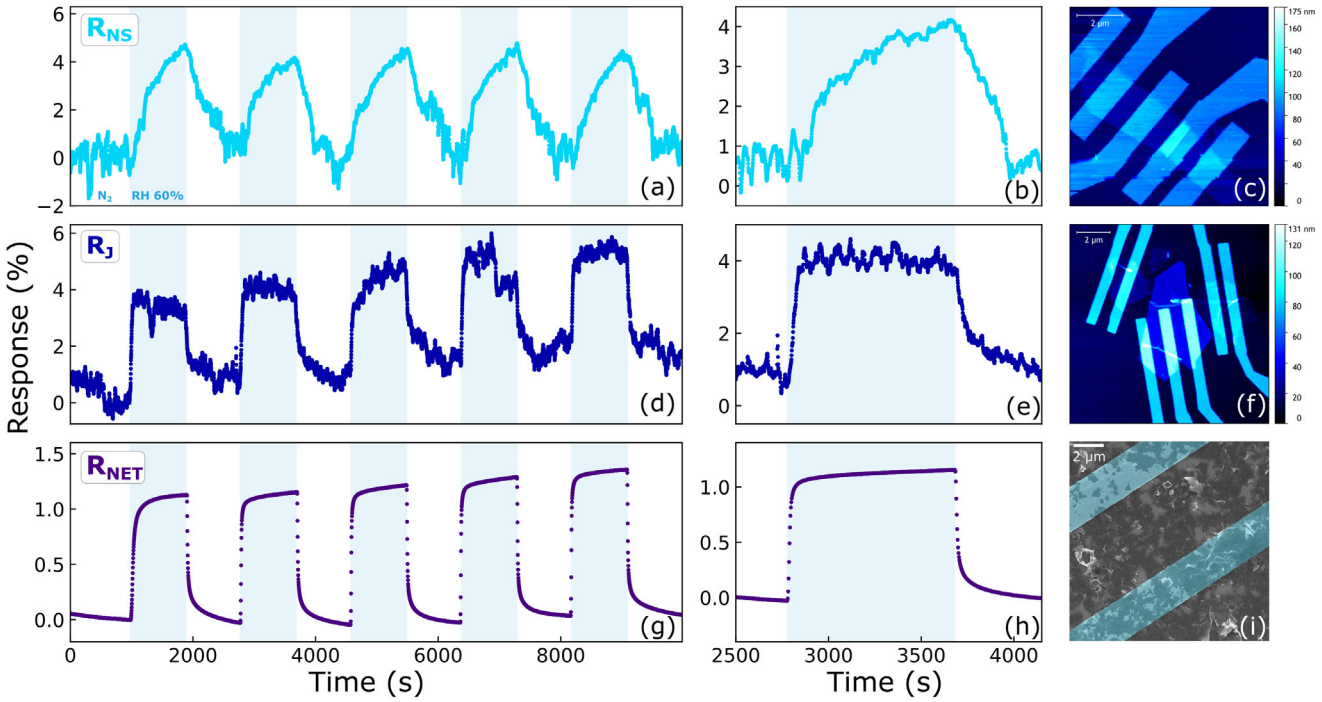

Figure 6 | Response of $Ti_3C_2T_x$ to humidity. Response of (a) an individual flake (R_{NS} = 10.5 kΩ - 2 contacts), (d) two flakes including a junction (R_J = 18.8 kΩ - 4 contacts), (g) a sensing layer deposited on interdigitated electrodes (R_{NET} = 126 Ω - 2 contacts) to 60% humidity in a N_2 environment. Each humidity pulse is indicated by light blue rectangles on the graphs. (b,e,c) Closer view of the responses to one humidity pulse. (c,f) AFM topography maps of the samples measured in (a) and (d) respectively. (i) SEM image of two of the digits covered with a layer of $Ti_3C_2T_x$, measured in (g).

network morphology such as flake lateral size, overlap area, thickness and stacking orientation.

3 | Conclusion

In summary, we studied charge transport through MXene conductive paths by decomposing the contributions to the total electrical resistance into individual flake resistances and junction resistances. Both contributions were independently measured with 4-probe STM, C-AFM and measurements on fabricated devices with contacts patterned on the $Ti_3C_2T_x$ flakes. It was possible to establish a quantitative (more than an order of magnitude) difference between junction resistances and flake resistances, as per the model of Gabbett et al. [4], using 4-probe measurements on devices and with multiple-probe STM. Those were carried out under different atmospheres including UHV, pure N_2 at ambient pressure, dry and humid air. We could experimentally confirm that inter-flake junction resistances are the main resistive component in MXene conductive paths, and that their values are strongly morphology-dependent. Additionally, we could image the junction resistances locally with STP and C-AFM, revealing a step-like change in the resistance at the junction location. With those measurements, it is possible to approximate charge transport in MXene conductive paths to a series of isopotential flakes and a sum of junction resistances. These findings are shedding light on charge transport in MXene layers with reliable experimental validation given the multi-technique approach used here. Gaining in-depth knowledge about nanoscale transport in $Ti_3C_2T_x$ is invaluable in the design of applications with MXene-network-based layers, due to the need for better control over their resistivity and reactivity to environmental changes. We illustrate the latter approach through the contrasting dynamics in the response of individual MXene flakes and of multi-junction network to humidity pulses.

4 | Methods

4.1 | $Ti_3C_2T_x$ Synthesis

$Ti_3C_2T_x$ is synthesized using the MILD (Minimally Intensive Layer Delamination) method, consisting in the etching of the "A" layer of a MAX precursor. In this case, Ti_3AlC_2 from Carbon Ukraine is used. The MILD method relies on the use of a milder etchant than concentrated HF: *in situ* HF. For this, 1.6 g of LiF salt (Sigma-Aldrich, 99%) is stirred with 20 mL HCl 9M (Sigma-Aldrich, 37 %) until full dissolution of the LiF. After, 1 g Ti_3AlC_2 is added slowly to the solution and kept under stirring in a Teflon beaker covered by a lid, and heated at 40 °C in an oil bath for 24 hours. As the reaction between the etchant and MAX phase is strongly exothermic, it is important to add the MAX powder very progressively to avoid heatpoints that damage the crystals. The delamination step takes place after the etching and consists in washing cycles with DI water. For this, several centrifugation steps are carried out at 6000 RPM for 5 minutes and repeated until the pH level of the supernatant approaches 7. The supernatant turns black, indicating the start of the delamination, and can be collected over 2-3 additional washing cycles. $Ti_3C_2T_x$ is obtained by collecting the slurry above the $Ti_3C_2T_x/Ti_3AlC_2$ sediment and filtering it by vacuum filtration using a 0.22 μ membrane filter. The obtained products are left to dry overnight

at room temperature, separated from the membrane filter and kept in an inert atmosphere to prevent oxidation. XRD, XPS, SEM and Raman characterizations are carried out directly on the dry, free-standing film obtained after filtration of the $Ti_3C_2T_x$ supernatant.

4.2 | Samples Fabrication

In order to deposit $Ti_3C_2T_x$ flakes on a Si/SiO_2 substrate, the dried products from the synthesis are dispersed in DI water by sonication for 1 minute. It is advised to keep the sonication time short as it can break the flakes or add defects. Deposition is performed by drop casting. The flake concentration on the substrate can be adjusted as a function of the time for which the droplet is in contact with the sample surface before being removed with a cleanroom wipe which can not touch the sample surface. Different flake concentration on the substrate are shown in the Supporting Information S6. The deposited flakes are then observed with optical microscopy to select the areas of interest. The samples intended for 4-probe STM are then stored under inert atmosphere, and the flakes of interest are measured with AFM in tapping mode to obtain more details about their topography.

The samples intended for full device fabrication go through more process steps. The contact patterns are created with electron beam lithography, on a spin-coated 200 nm PMMA layer. Then follows a development in IPA:MIBK after which metallic layers are deposited by thermal evaporation. A 5 nm Ti adhesion layer and a 55 nm Au layer were deposited. Lift-off was carried out with acetone, and the as-fabricated devices were imaged with optical microscopy and AFM in tapping mode to validate the contact geometry. After validation, the samples were glued and wire bonded on DIL16 sockets.

4.3 | 4-Probe STM

4-probe measurements on $Ti_3C_2T_x$ are carried out in a multiple probe STM system, in a UHV environment, with prior preparation of the tungsten tips and the sample. The tips were placed under SEM visualization to ensure the landing of the tip on $Ti_3C_2T_x$ and not on the SiO_2 surface. When all four tips are in contact, it is then possible to perform four-contact measurements by applying a given current to the two external probes and measuring the voltage drop between the two inner probes. SEM visualization also allows to measure the effective distance between the probes.

The multiple probe STM is also used to perform STP, in which three tips are used. Again, the two external probes apply a given current through the sample, and the third tip is scanning the surface of the sample. The scan produces a map of the sample topography and a map of the voltage potential, simultaneously acquired.

4.4 | C-AFM

C-AFM measurement were carried out in ambient conditions, with a Bruker Icon Dimension equipped with a C-AFM module. SCM-PIT-V2 tips (Bruker) were used for the measurements. The force applied by the tip was maintained around 100 nN. It is worth note that the C-AFM current measured on the flakes is force-dependent below 60 nN, as depicted in Figure S6a,b (Supporting Information). Gwyddion was used for C-AFM data analysis.

4.5 | Measurements on Fabricated Devices

All of the measurements carried out on the fabricated devices were done using one or several lock-in amplifiers (MFLI, Zurich Instruments). This configuration allowed measurement of very conductive samples while keeping low current values as the samples are quite fragile given their size. The lock-in amplifiers were used at 117 Hz with a current below 20 nA going through the samples. Those measurements are carried out in both ambient air and controlled atmosphere. For the latter, a specific setup is used, in which a gas chamber is fixed on the measuring PCB and connected to gas lines. In this case, measurements were done with nitrogen and various humidity levels, generated by a bubbler and measured by a Winsen reference sensor. The gas flux is kept constant at 1000 mL/min, using mass flow controls on the gas lines.

Acknowledgments

B.H. (senior research associate) is supported by the F.R.S.-FNRS. The authors are grateful to the Walloon region for funding this research through SIAHNA project. The authors also acknowledge financial support from the ARC project DREAMS (21/26.116) and from the FNRS Research Credit (CDR) "CANOE." The authors also thank the IEMN-PCMP-PCP platform and Renatech network. The authors thank Cécile D'Haese and Benoît Hubert for their support, as well as VOCSens team for the collaboration and technical support. The support of Jean-François Statsyns, Pierre Eloy and François Devred is also sincerely acknowledged.

Conflicts of Interest

The authors declare no conflict of interest.

Data Availability Statement

The data that support the findings of this study are available from the corresponding author upon reasonable request.

References

1. B. Tang, M. Sivan, J. F. Leong, et al., "Solution-Processable 2D Materials for Monolithic 3D Memory-Sensing-Computing Platforms: Opportunities and Challenges," *npj 2D Materials and Applications* 8, no. 1 (2024): 74.

2. C. Gabbett, L. Doolan, K. Synnatschke, et al., "Quantitative Analysis of Printed Nanostructured Networks Using High-Resolution 3D FIB-SEM Nanotomography," *Nature Communications* 15, no. 1 (2024): 278.

3. B. Favelukis, B. Ratzker, Y. Juhl, et al., "Selective Wet Etching for Scalable Nanofabrication of Patterned MXene Thin Films," *Nano Letters* (2025).

4. C. Gabbett, A. Kelly, E. Coleman, et al., "Understanding How Junction Resistances Impact the Conduction Mechanism in Nano-Networks," *Nature Communications* 15 (2024): 4517.

5. E. Coleman, L. Doolan, A. Dawson, et al., "Decoupling Junction and Nanosheet Transport in Graphene Networks via Simple DC Temperature-Dependent Measurements," *Small* 21 (2025): e09314.

6. M. Naguib, M. Kurtoglu, V. Presser, et al., "Two-Dimensional Nanocrystals Produced by Exfoliation of Ti_3AlC_2," *Advanced Materials* 23 (2011): 4248–4253.

7. M. Schied, H. Pazniak, F. Brette, et al., "Reactivity of $Ti_3C_2T_x$ MXene With Atomic Hydrogen: Tuning of Surface Terminations by Halogen Removal and Reversible O to OH Conversion," *Chemistry of Materials* 36, no. 24 (2024): 11 905–11 919.

8. A. Iqbal, T. Hassan, Z. Gao, F. Shahzad, and C. M. Koo, "MXene-Incorporated 1D/2D Nano-Carbons for Electromagnetic Shielding: A Review," *Carbon* 203 (2022): 542–560.

9. X. Li, H. Zhaodong, C. Shuck, G. Liang, Y. Gogotsi, and C. Zhi, "MXene Chemistry, Electrochemistry and Energy Storage Applications," *Nature Reviews Chemistry* 6 (2022): 389–404.

10. A. Iqbal, T. Hassan, S. Madad, Y. Gogotsi, and C. M. Koo, "MXenes for Multispectral Electromagnetic Shielding," *Nature Reviews Electrical Engineering* 1 (2024): 180–198.

11. Y. Li, S. Huang, S. Peng, et al., "Toward Smart Sensing by MXene," *Small* 19, no. 14 (2023): 2206126.

12. O. de Leuze, F. M. Fernandes, S. Arib, et al., "Anisotropic Charge Transport in 2D Single Crystals of $Ti_3C_2T_x$ MXenes," *Communications Materials* 6, no. 1 (2025): 186.

13. M. Barsoum and Y. Gogotsi, "Removing Roadblocks and Opening New Opportunities for MXenes," *Ceramics International* 49 (2022): 24112–24122.

14. P. N. Nirmalraj, P. E. Lyons, S. De, J. N. Coleman, and J. J. Boland, "Electrical Connectivity in Single-Walled Carbon Nanotube Networks," *Nano Letters* 9, no. 11 (2009): 3890–3895.

15. S. Sahare, P. Ghoderao, P. Yin, et al., "An Assessment of MXenes Through Scanning Probe Microscopy," *Small Methods* 6, no. 6 (2022): 2101599.

16. Z. Hemmat, P. Yasaei, J. Schultz, et al., "Tuning Thermal Transport Through Atomically Thin Ti3C2Tz MXene by Current Annealing in Vacuum," *Advanced Functional Materials* 29 (2019): 1805693.

17. M. Shekhirev, J. Busa, C. E. Shuck, et al., "Ultralarge Flakes of $Ti_3C_2T_x$ MXene via Soft Delamination," *ACS Nano* 16, no. 9 (2022): 13 695–13 703.

18. A. Lipatov, A. Goad, M. J. Loes, et al., "High Electrical Conductivity and Breakdown Current Density of Individual Monolayer $Ti_3C_2T_x$ MXene Flakes," *Matter* 4, no. 4 (2021): 1413–1427.

19. A. Lipatov, S. Bagheri, and A. Sinitskii, "Metallic Conductivity of $Ti_3C_2T_x$ MXene Confirmed by Temperature-Dependent Electrical Measurements," *ACS Materials Letters* 6, no. 1 (2023): 298–307.

20. X. Sang, Y. Xie, M.-W. Lin, et al., "Atomic Defects in Monolayer Titanium Carbide ($Ti_3C_2T_x$) MXene," *ACS Nano* 10 (2016): 9193–9200.

21. A. Lipatov, M. Alhabeb, M. R. Lukatskaya, A. Boson, Y. Gogotsi, and A. Sinitskii, "Effect of Synthesis on Quality, Electronic Properties and Environmental Stability of Individual Monolayer Ti3C2 MXene Flakes," *Advanced Electronic Materials* 2, no. 12 (2016): 1600255.

22. M. J. Loes, S. Bagheri, and A. Sinitskii, "Layer-Dependent Gas Sensing Mechanism of 2D Titanium Carbide ($Ti_3C_2T_x$) MXene," *ACS Nano* 18, no. 38 (2024): 26 251–26 260.

23. M. Benchakar, L. Loupias, C. Garnero, et al., "One MAX Phase, Different MXenes: A Guideline to Understand the Crucial Role of Etching Conditions on $Ti_3C_2T_x$ Surface Chemistry," *Applied Surface Science* 530 (2020): 147209.

24. M. Mičušík, M. Šlouf, A. Stepura, Y. Soyka, E. Ovodok, M. Prochazka, and M. Omastova, "Aging of 2D MXene Nanoparticles in Air: An XPS and TEM Study," *Applied Surface Science* 610 (2023): 155351.

25. P. Muralt and D. W. Pohl, "Scanning Tunneling Potentiometry," *Applied Physics Letters* 48, no. 8 (1986): 514–516.

26. J. Pešić, S. Leitner, J. Neilson, et al., "Imaging Junctions in Two-Dimensional Semiconductor Nanosheet Networks," *npj 2D Materials and Applications* 9, no. 1 (2025): 1–9.

27. E. Piatti, A. Arbab, F. Galanti, et al., "Charge Transport Mechanisms in Inkjet-Printed Thin-Film Transistors Based on Two-Dimensional Materials," *Nature Electronics* 4, no. 12 (2021): 893–905.

28. S. Tangui, S. Hurand, R. Aljasmi, et al., "2D Versus 3D-Like Electrical Behavior of MXene Thin Films: Insights from Weak Localization in the Role of Thickness, Interflake Coupling and Defects," *Small* 21, no. 1 (2025): 2406334.

29. P. G. Slade, *Electrical Contacts: Principles and Applications* (CRC Press, 2017).

30. T. Hu, H. Zhang, J. Wang, et al., "Anisotropic Electronic Conduction in Stacked Two-Dimensional Titanium Carbide," *Scientific Reports* 5 (2015): 16329.

31. O. Niksan, B. C. Wyatt, K. K. Kazemi, B. Anasori, and M. H. Zarifi, "MXene Free Standing Films: Unlocking the Impact of Flake Sizes in Microwave Resonant Structures in Humid Environments," *Small* 19, no. 37 (2023): 2300848.

32. T. Guo, D. Zhou, S. Deng, et al., "Rational Design of $Ti_3C_2T_x$ MXene Inks for Conductive, Transparent Films," *ACS Nano* 17, no. 4 (2023): 3737–3749.

33. Y. Yuan and M. Lanza, "The Effect of Relative Humidity in Conductive Atomic Force Microscopy," *Advanced Materials* 36, no. 51 (2024): 2405932.

34. M. R. Vazirisereshk, S. A. Sumaiya, R. Chen, M. Z. Baykara, and A. Martini, "Time-Dependent Electrical Contact Resistance at the Nanoscale," *Tribology Letters* 69, no. 2 (2021): 50.

35. S. Yu, P. Li, H. Ding, C. Liang, and X. Wang, "2D MXenes-Based Gas Sensors: Progress, Applications, and Challenges," *Small Methods* 9 (2025): 2402179.

36. S. Patra, N. U. Kiran, P. Mane, B. Chakraborty, L. Besra, S. Chatterjee, and S. Chatterjee, "Hydrophobic MXene With Enhanced Electrical Conductivity," *Surfaces and Interfaces* 39 (2023): 102969.

37. Y. Wang, J. Fu, J. Xu, H. Hu, and D. Ho, "Atomic Plasma Grafting: Precise Control of Functional Groups on $Ti_3C_2T_x$ MXene for Room Temperature Gas Sensors," *ACS Applied Materials & Interfaces* 15, no. 9 (2023): 12 232–12 239.

38. K. Cheng, X. Tian, S. Yuan, Q. Feng, and Y. Wang, "Research Progress on Ammonia Sensors Based on $Ti_3C_2T_x$ MXene at Room Temperature: A Review," *Sensors (Basel, Switzerland)* 24, no. 14 (2024): 4465.

39. H. An, T. Habib, S. Shah, et al., "Water Sorption in MXene/Polyelectrolyte Multilayers for Ultrafast Humidity Sensing," *ACS Applied Nano Materials* 2, no. 2 (2019): 948–955.

40. W. Waheed, S. Anwer, M. U. Khan, M. Sajjad, and A. Alazzam, "2D $Ti_3C_2T_x$-MXene Nanosheets and Graphene Oxide Based Highly Sensitive Humidity Sensor for Wearable and Flexible Electronics," *Chemical Engineering Journal* 480 (2024): 147981.

Supporting Information

Additional supporting information can be found online in the Supporting Information section.

Supporting File: smll73012-sup-0001-SuppMat.pdf.